Supplementary Information

Interlayer chemical confinement enables highly reversible and durable lithium–chlorine batteries

Baoquan Liu[a], Yanzeng Ge[a], Changfeng Lin[a], Haizhen Jiang[a], Tianyu Qiu[a], Jing Li[a], Hui Zhang[a], Jinlin Yang[a,*], and Xinlong Tian[a,*]

[a] *State Key Laboratory of Tropic Ocean Engineering Materials and Materials Evaluation, Hainan Provincial Key Lab of Fine Chem, Hainan University, Haikou 570228, China*

***Corresponding author:**

tianxl@hainanu.edu.cn (X. Tian)

yangjl@hainanu.edu.cn (J. Yang)

Experimental section

Chemicals and reagents

Ti_3AlC_2 (400 meshes) was purchased from xinxi Tech Co., Ltd. $CuCl_2$ (anhydrous, 98%), AgCl (anhydrous, 99.99%), CuI (anhydrous, 99.99%), S powder (300 mesh, 99.9%), Se powder (300 mesh, 99.9%), Te powder (300 mesh, 99.9%), NaCl (anhydrous, 99.5%), KCl (anhydrous, 99.5%), LiCl (99%), $AlCl_3$ (99 %), $SOCl_2$ (99%, Aladdin), $NH_3 \cdot H_2O$ (GR, 25-28%), NH_4Cl (GR, 99.5%), TBAOH (25% solution) were purchased from Aladdin. LiFSI (99 %) and LiTFSI (99 %) were purchased from DoDoChem Co., Ltd. Super P and PVDF were purchased from Canrd Technology Co., Ltd.

Preparation of MXenes

A chemical scissor–mediated structural editing route was used to synthesize the S-, Se-, and Te-teminated MXenes. Specifically, Ti_3AlC_2 precursor, chemical scissor ($CuCl_2$, AgCl, and CuI for S-, Se-, and Te-teminated MXenes, respectively), intercalant (S, Se, and Te for S-, Se-, and Te-teminated MXenes, respectively), and NaCl-KCl salts were mixed in a molar ratio of 1:3:1:2 and ground in a mortar under the argon protection for 10 min. The mixture was then placed in a corundum boat and transferred to a tightly sealed tube furnace with an argon flow (100 sccm). The synthesis reactions of three samples were carried out at 700 °C and held for 24 h. The product was then washed with a 2 M NH_4Cl and $NH_3 \cdot H_2O$ mixed solution (volume ratio of 1:1) to eliminate the metal particles produced. The obtained product was further washed with deionized water before being dried in a vacuum oven at 40 °C for 24 h.

$Ti_3C_2S_x$ nanosheets were obtained via an intercalation-exfoliation method. Specifically, 0.2 g of $Ti_3C_2S_x$ multilayer powder was added to 10 mL of TBAOH (25%) aqueous solution under Ar gas and stirred overnight. The obtained colloidal MXene suspension was then centrifuged at 15000 rpm with a large excess of water to completely separate the intercalated powder from the liquid TBAOH. Deionized water was subsequently added to the residual MXenes and then ultrasonicated for 6 h at low temperature (ice bath) to limit oxidation. Then, the TBAOH-treated $Ti_3C_2S_x$ was centrifuged at 3500 rpm for 20 min to eliminate the sediment. After the elimination of the precipitate, the exfoliated MXene was obtained via vacuum freeze-drying for 2 days.

Preparation of $SOCl_2$-based electrolyte

Electrolyte was prepared in an Ar-filled glovebox with H_2O and O_2 content <0.01 ppm. Firstly, 0.532 g of $AlCl_3$ powder was added into 2 mL of $SOCl_2$ solution and stirred until the $AlCl_3$ was fully dissolved. Subsequently, 0.168 g of LiCl, 0.088 g of LiFSI, and 0.088 g of LiTFSI powder were added to the above $AlCl_3$-$SOCl_2$ solution and stirred until complete dissolution.

Electrochemical measurements

The MXene cathodes were prepared by mixing MXene powder, carbon black (Super P), and polyvinylidene difluoride (PVDF) in a weight ratio of 8:1:1 in N-Methylpyrrolidone (NMP), followed by coating onto nickel foam and vacuum drying (80 °C, 12 h). The cathode mass loading was controlled at

1.5~2.0 mg cm^{-2}. The battery assembly was performed in an Ar-filled glovebox with H_2O and O_2 content <0.01 ppm. For Swagelok cell, 12 mm diameter of MXene cathode and Li anode discs were used. The pouch cell was constructed with a single-layer structure. The sizes of the cathode and anode are 4 × 5 cm^2. The electrode tabs and the tabs with the Al soft packaging films were bonded by the tab film via hot-pressing. The sealing procedure was conducted by the automated vacuum sealing machine. Glass fibers (Whatman, GF/D) was employed as separator for both Swagelok- and pouch-type cells. The galvanostatic cycling were carried out on a battery-testing instrument (LAND CT3002A). The cyclic voltammetry (CV) and electrochemical impedance spectroscopy (EIS) were performed on an electrochemical workstation (CHI 760E). The galvanostatic intermittent titration technique (GITT) involved the application of constant current pulses for 5 min at 1 A g^{-1} followed by a 60-min open-circuit voltage relaxation period.

Materials characterization

The crystal structures of the samples were examined by XRD (Rigaku D/Max 2400) with a Cu-Kα radiation source (λ = 1.5406 Å). The morphology and microstructure characterizations were performed by scanning electron microscopy (SEM, Thermo-Scientific Quattro S) equipped with energy dispersive X-ray spectroscopy (EDS). The atomic structural analysis was performed by using the high-angle annular dark-field scanning transmission electron microscopy (HAADF-STEM; Titan Themis Z 3.1, FEI Company, USA) at 300 kV. The samples for STEM were prepared by a focused ion beam (FIB, HELIOS NanoLab 600i, FEI Company, USA). The surface chemical states of the samples was performed on X-ray photoelectron spectroscopy (XPS, Thermo-Scientific ESCALAB Xi+). Time-of-flight secondary ion mass spectrometry (TOF-SIMS) measurements were conducted on a TOF.SIMS 5-100 instrument (IONTOF GmbH). The analysis chamber was maintained under ultra-high vacuum (< 2 × 10^{-9} mbar). Depth profiling analysis was performed by sputtering with a Cs^+ beam (2 keV, 110 nA), and the studied area had a size of 45 × 40 μm^2. Gas chromatography-mass spectrometry (GC-MS) measurement was conducted using an Agilent 7890B+7000B system. The charged and discharged electrodes were disassembled in an argon-filled glovebox and immediately placed into a 20 mL of headspace vial. The vial was then connected to the instrument. The headspace sampler was heated to 80°C and maintained in the oven for 30 minutes. After equilibration, the gas was automatically injected into the GC-MS system for analysis.

In situ Raman experiment was performed on a Raman spectrometer (RENISHAW) with an excitation laser wavelength of 532 nm. The top of the in situ Raman cell was constructed using a quartz window. Two 3 mm hole was punched on the Li anode and separator to allow the Raman laser to excite the cathode on the other side.

In situ XRD experiment was performed on a Rigaku D/Max 2400 system with a Cu-Kα radiation source. The top of the in situ cell was constructed using a polyimide window. The $Ti_3C_2S_x$ cathode was placed on the back of the Polyimide window, separated from the Li anode by a glass fiber with 100 μL electrolyte. The XRD patterns were collected within the 2θ range of 20-60° at intervals of 5 minutes.

Computational methods

Density functional theory calculations were performed using the Perdew-Burke-Ernzerhof (PBE)[15] functional and the projector augmented wave (PAW)[16,17] potential as implemented in the Vienna Ab Initio Simulation Package (VASP).[18,19] An energy cutoff of 450 eV and a convergence criterion of 10^{-5} eV for self-consistent calculations was adopted. All structures were fully relaxed until the total force on each atom was less than 0.05 eV/Å. A supercell of $Ti_3C_2T_x$ was set to 3 × 3 × 1. A Γ-centered 3 × 3 × 1 k-point was adopted during the constructure optimization, and 5 × 5 × 1 k-point was employed during the electronic structure calculations. The DFT-D3 method with Becke-Jonson damping is used to add vdW dispersion correction.[20] VASPKIT code[21] and VESTA software[22] were used for calculation pre-processing and post-processing. COMSOL Multiphysics software was used to simulate the Li^+ ion distribution on the electrode. The simulation used Butler−Volmer expression to describe the reaction kinetics of all electrodes and the flux of each ion was calculated by the Nernst−Planck formulation. In the model cell, the length and width are set to 5.4 and 4.8 μm, respectively. The initial Li^+ ion concentration was set to 1 M.

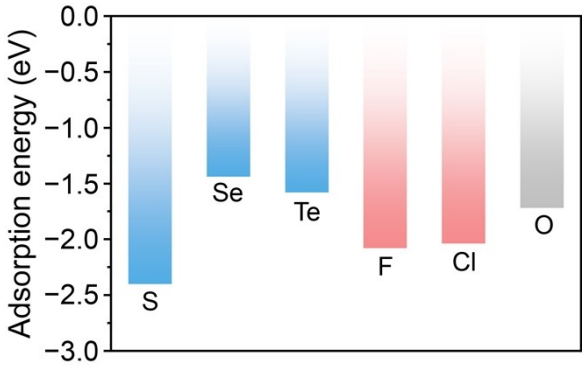

Figure S1. Adsorption energies of Cl_2 molecule on the $Ti_3C_2T_x$ MXenes with different terminations.

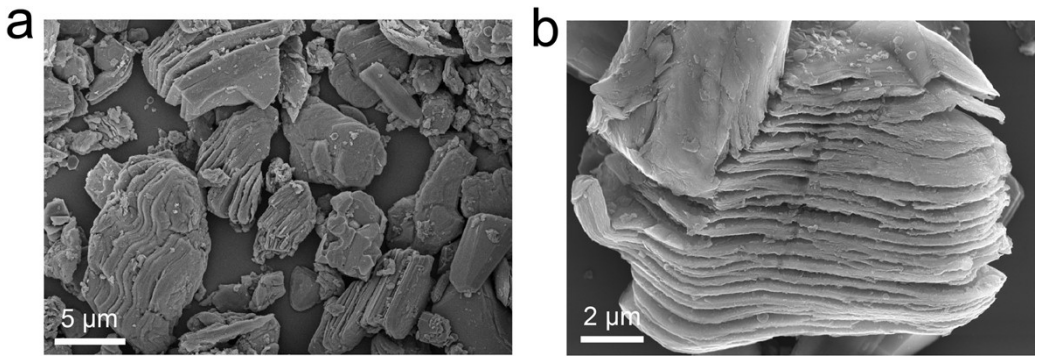

Figure S2. SEM images of $Ti_3C_2S_x$.

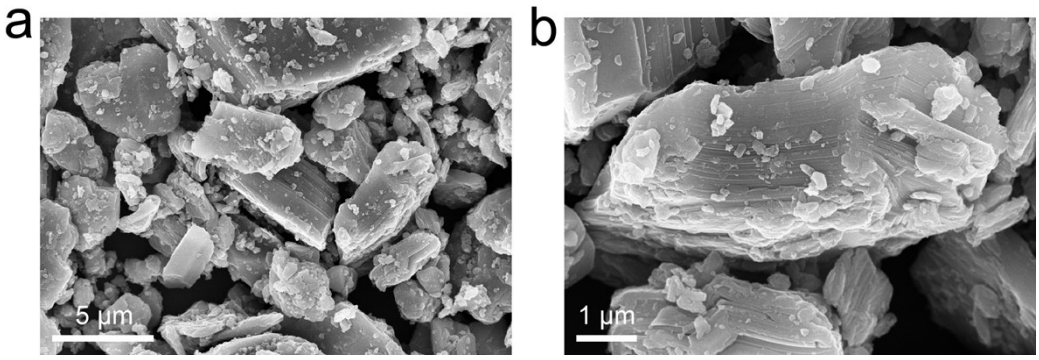

Figure S3. SEM images of Ti_3AlC_2 phases.

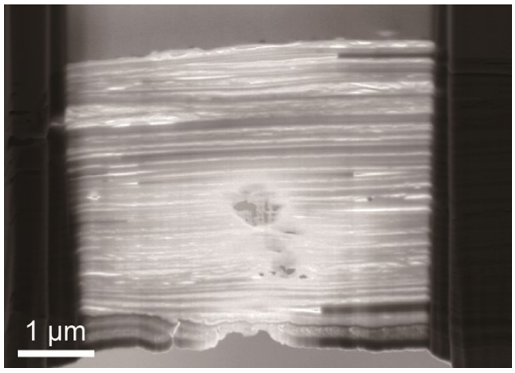

Figure S4. SEM image of the cross-sectional slice prepared by focused ion beam machining.

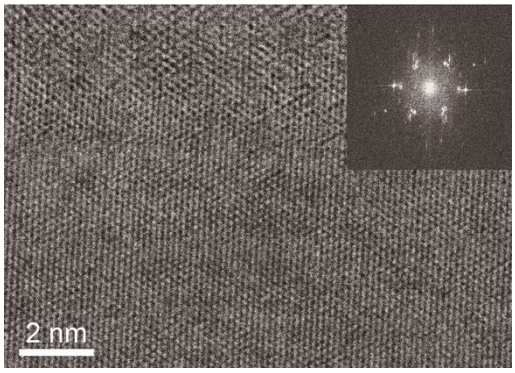

Figure S5. HAADF-STEM image recorded for $Ti_3C_2S_x$ along the [0001] zone axis and the corresponding fast Fourier transform pattern.

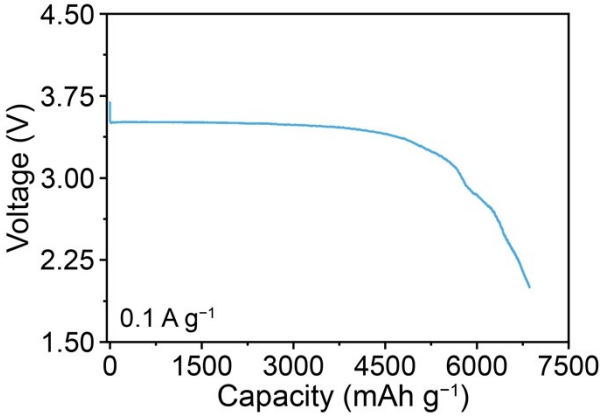

Figure S6. The first discharge curve of Li–Cl_2@$Ti_3C_2S_x$ battery.

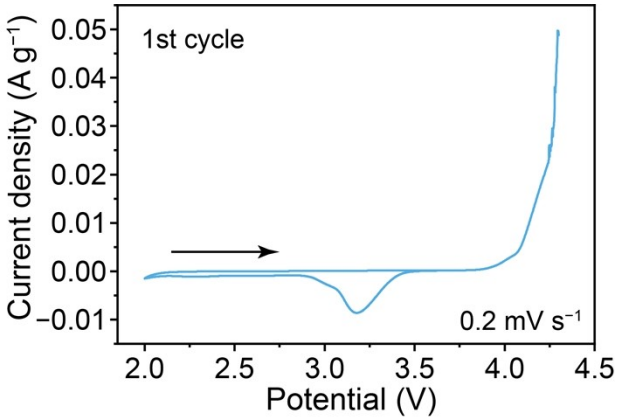

Figure S7. CV curve of the Li–Cl_2@$Ti_3C_2S_x$ battery with a scan rate of 0.2 mV s^{-1}.

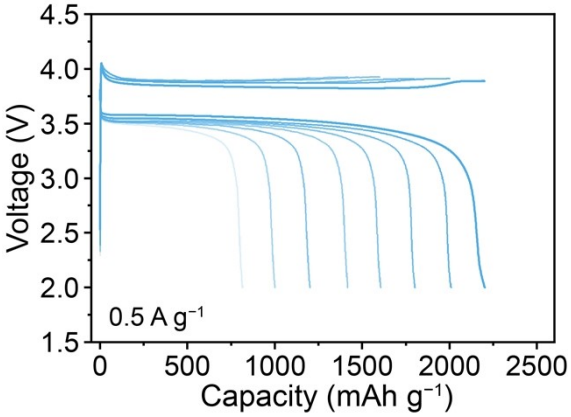

Figure S8. The voltage–capacity profiles of the Li–Cl_2@$Ti_3C_2S_x$ battery under charge capacities of 800–2200 mAh g^{-1} at a current density of 0.5 A g^{-1}.

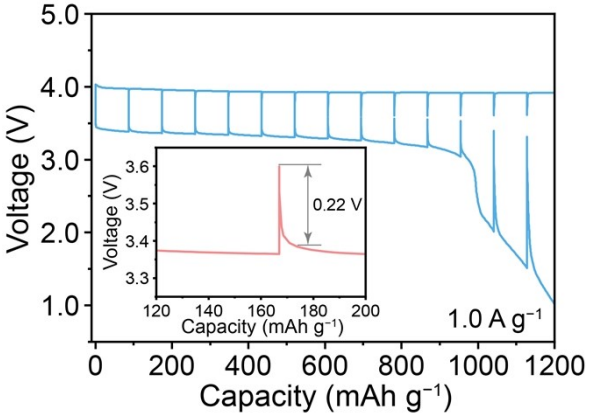

Figure S9. GITT curve of the Li–Cl_2@$Ti_3C_2S_x$ battery.

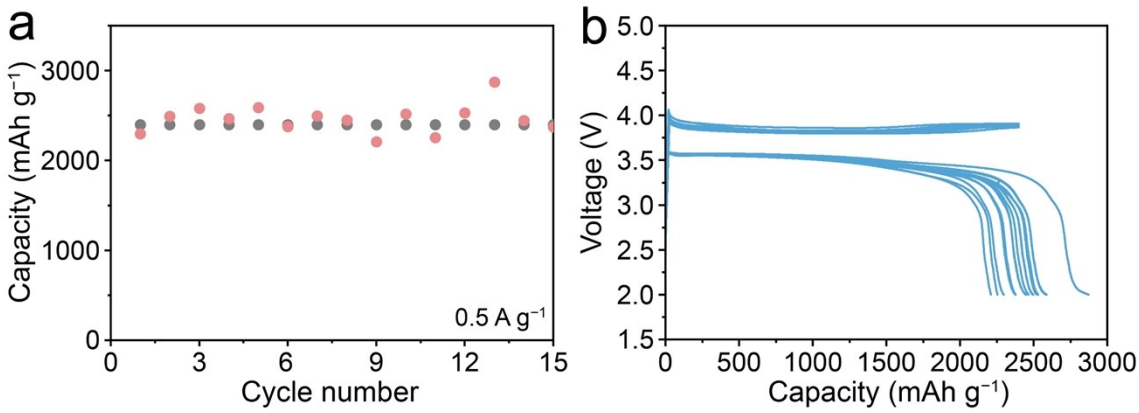

Figure S10. Cycling performance of the Li–Cl_2@$Ti_3C_2S_x$ battery under charge capacities of 2400 mAh g^{-1} at a current density of 0.5 A g^{-1}.

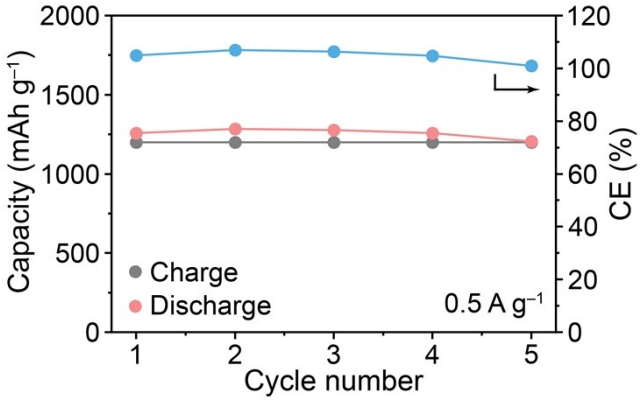

Figure S11. Cycling tests of the Li–Cl_2@$Ti_3C_2S_x$ battery for the first 5 cycles at 0.5 A g^{-1}.

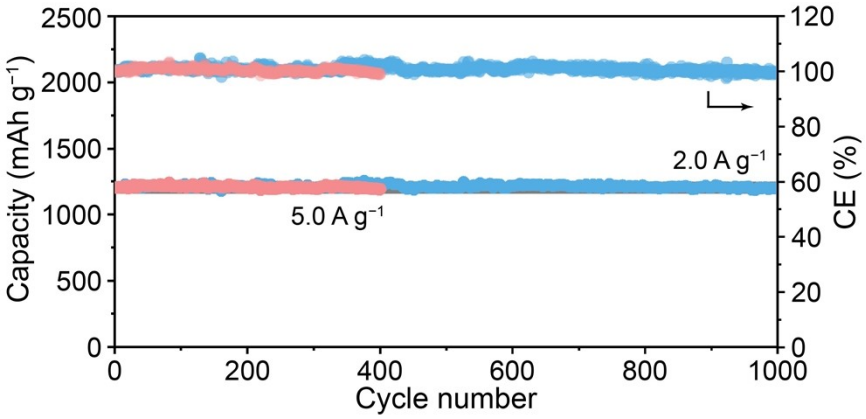

Figure S12. Cycling performances of the Li–Cl_2@$Ti_3C_2S_x$ battery at current densities of 2.0 and 5.0 A g^{-1}.

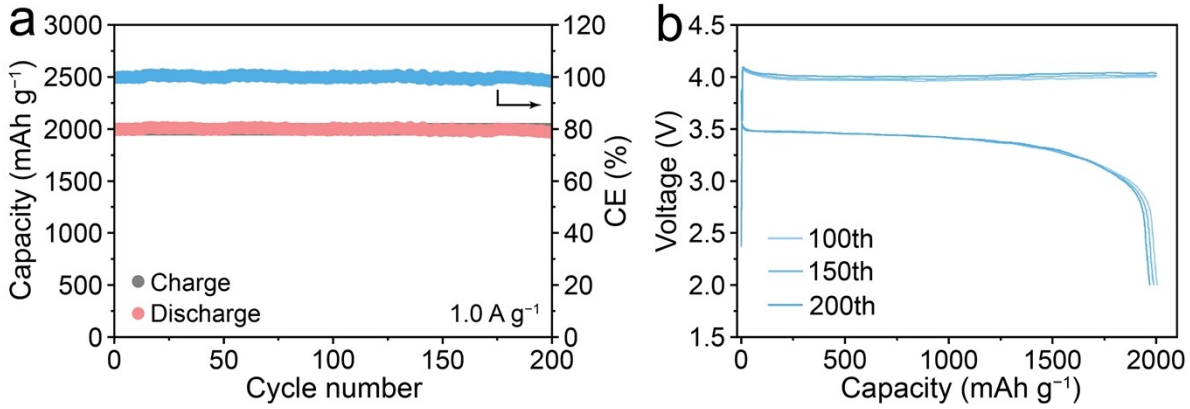

Figure S13. (a) Cycling performance of the Li–Cl_2@$Ti_3C_2S_x$ battery at charge capacity of 2000 mAh g^{-1} and (b) the corresponding voltage–capacity profiles in different cycles.

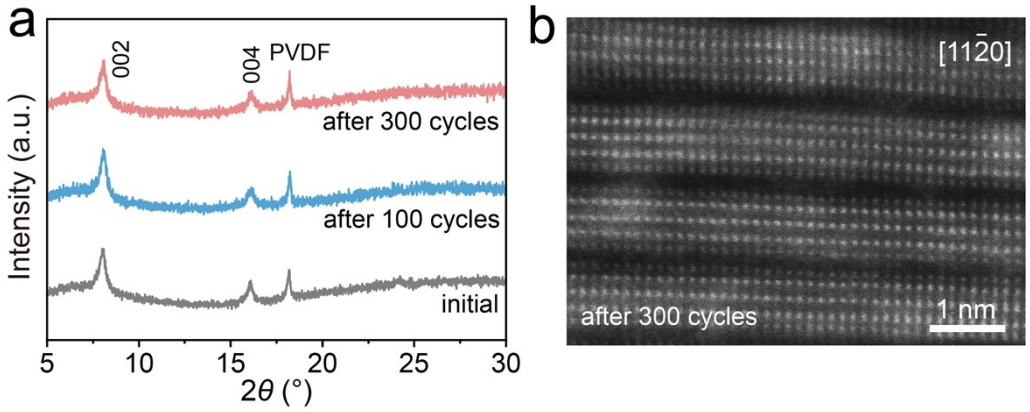

Figure S14. (a) XRD patterns and (b) HAADF-STEM image of $Ti_3C_2S_x$ electrodes after different cycles.

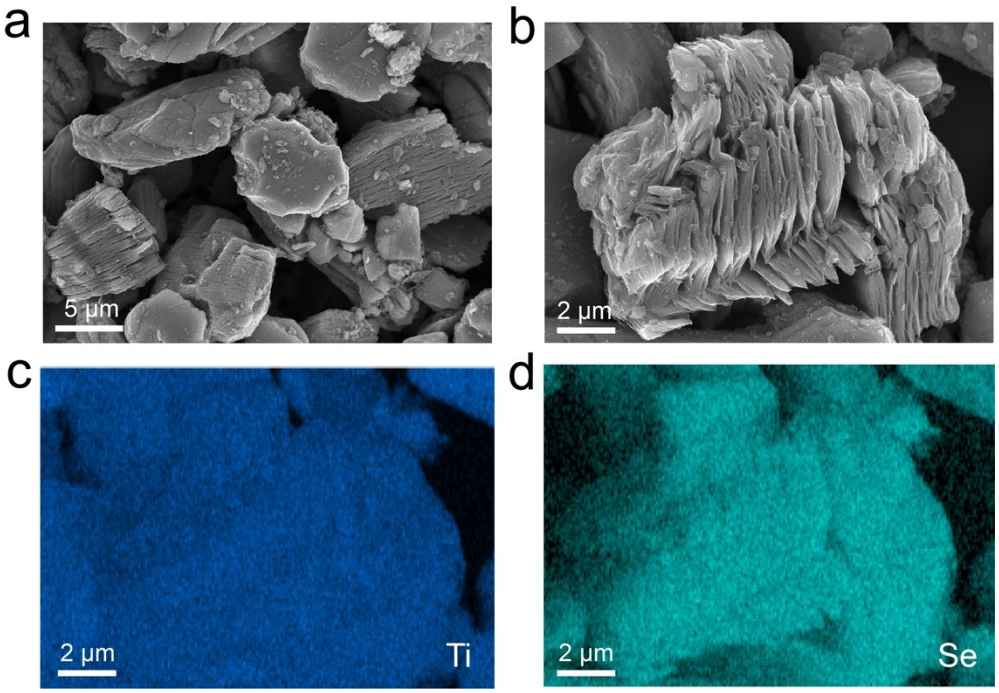

Figure S15. (a–b) SEM images of the $Ti_3C_2Se_x$ MXene and the corresponding elemental mapping images for (c) Ti and (d) Se.

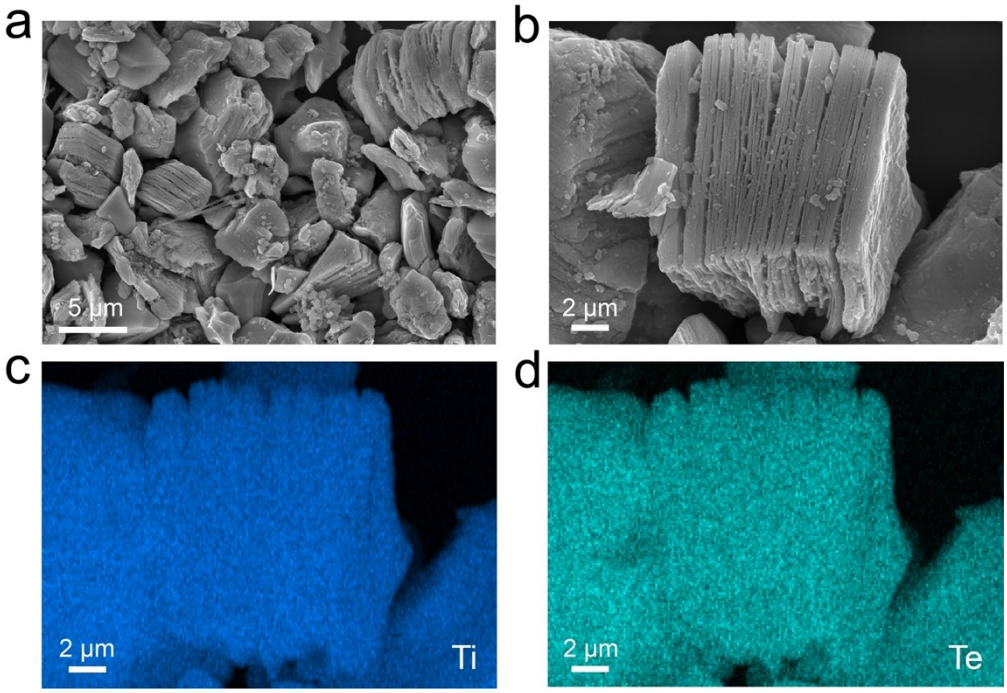

Figure S16. (a–b) SEM images of the $Ti_3C_2Te_x$ MXene and the corresponding elemental mapping images for (c) Ti and (d) Te.

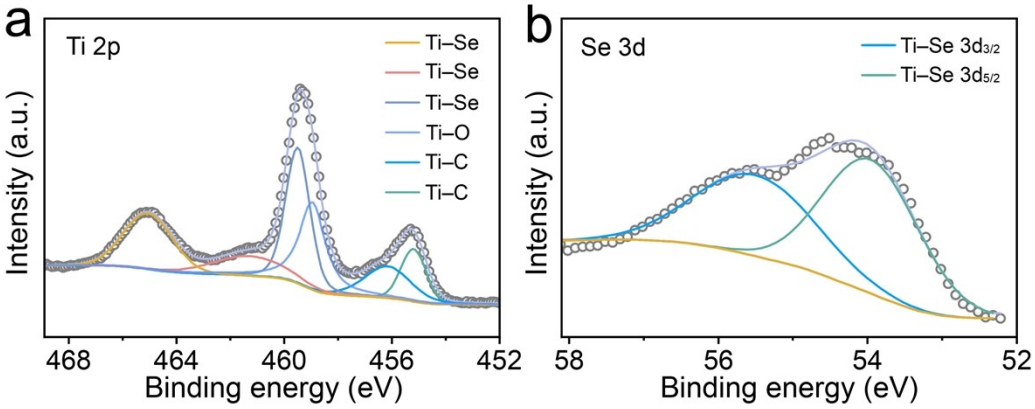

Figure S17. High-resolution (a) Ti 2p and (b) Se 3d XPS spectra recorded for $Ti_3C_2Se_x$.

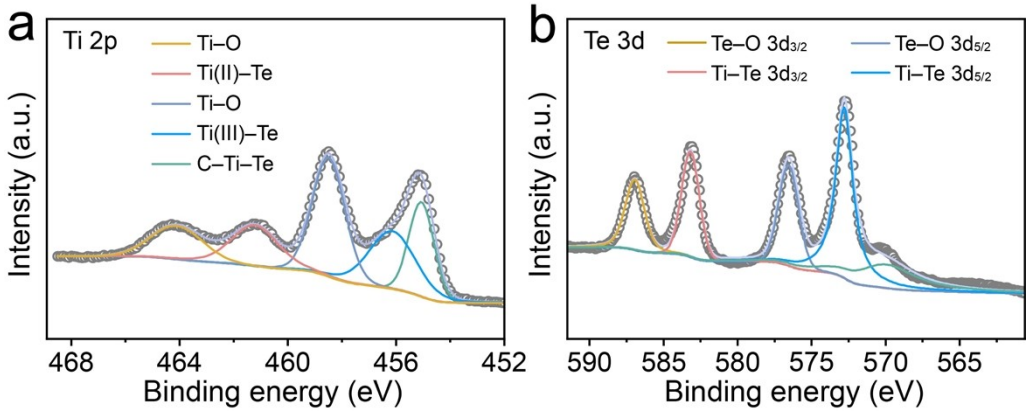

Figure S18. High-resolution (a) Ti 2p and (b) Te 3d XPS spectra recorded for $Ti_3C_2Te_x$.

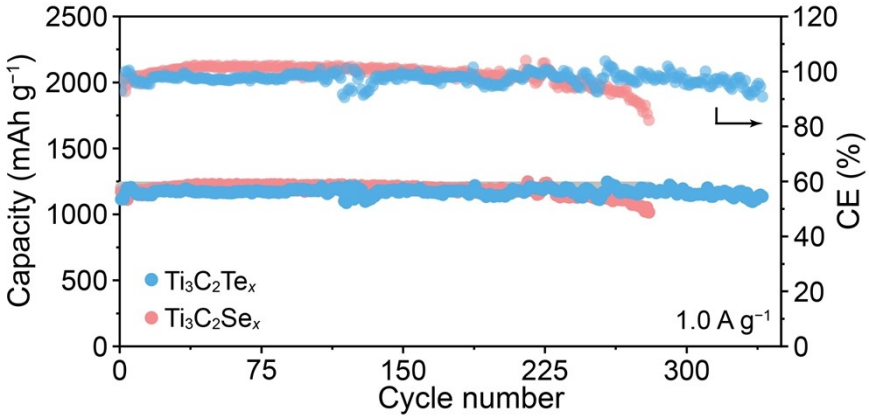

Figure S19. Cycling performances of the Li–Cl_2@$Ti_3C_2Se_x$ and Li–Cl_2@$Ti_3C_2Te_x$ batteries at current density of 1.0 A g^{-1}.

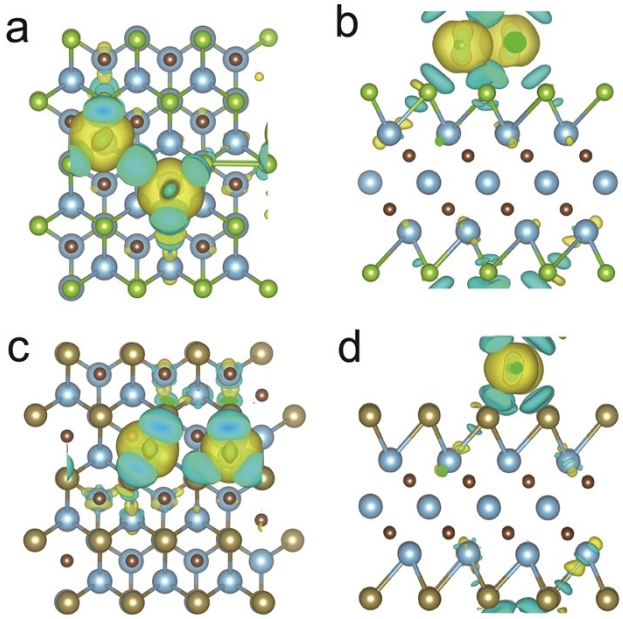

Figure S20. Electron density difference mapping of a Cl atom adsorbed on (a–b) $Ti_3C_2Se_x$, (c–d) $Ti_3C_2Te_x$.

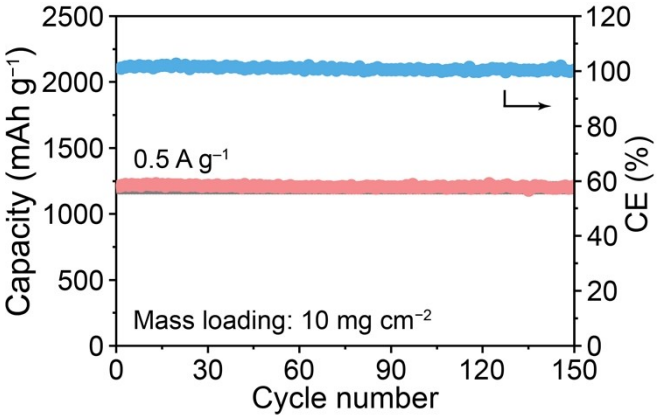

Figure S21. Cycling performance of the Li–Cl_2@$Ti_3C_2S_x$ battery under high mass loading of 10 mg cm^{-2}.

Figure S22. Digital photograph the Li–Cl_2@$Ti_3C_2S_x$ pouch cell after 50 cycles.

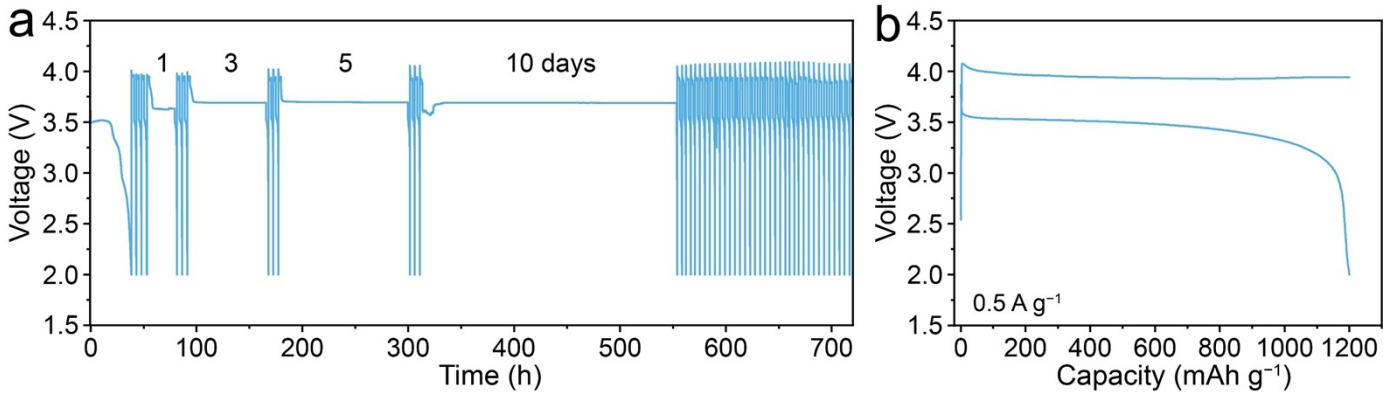

Figure S23. (a) Retention capability of the Li–Cl_2@$Ti_3C_2S_x$ battery at room temperature. (b) Voltage–capacity profile of the battery after a retention period of 19 days.

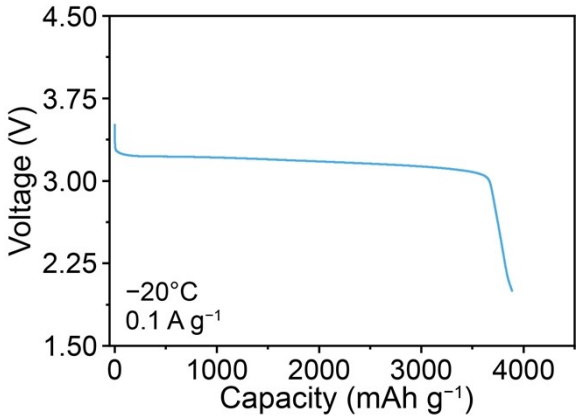

Figure S24. The first discharge curve of Li–Cl_2@$Ti_3C_2S_x$ battery at −20 °C.

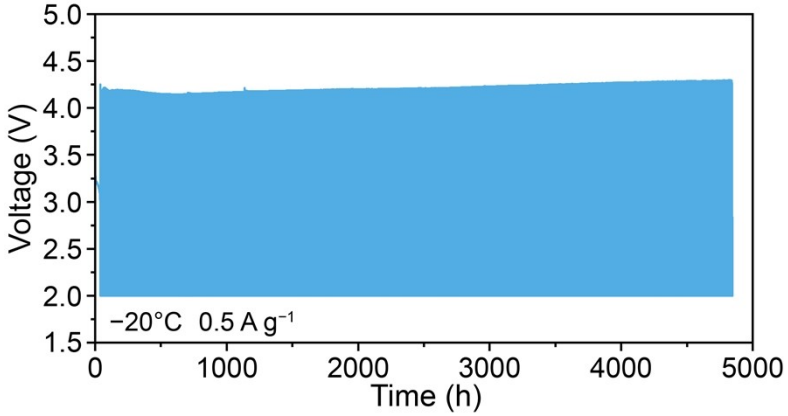

Figure S25. Voltage–time curve of the Li–Cl_2@$Ti_3C_2S_x$ battery at −20 ℃.

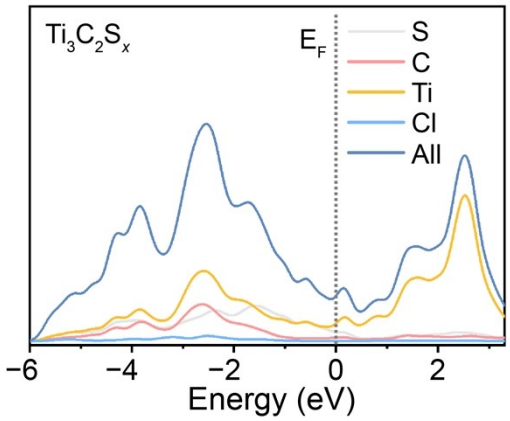

Figure S26. Calculated density of states for $Ti_3C_2S_x$.

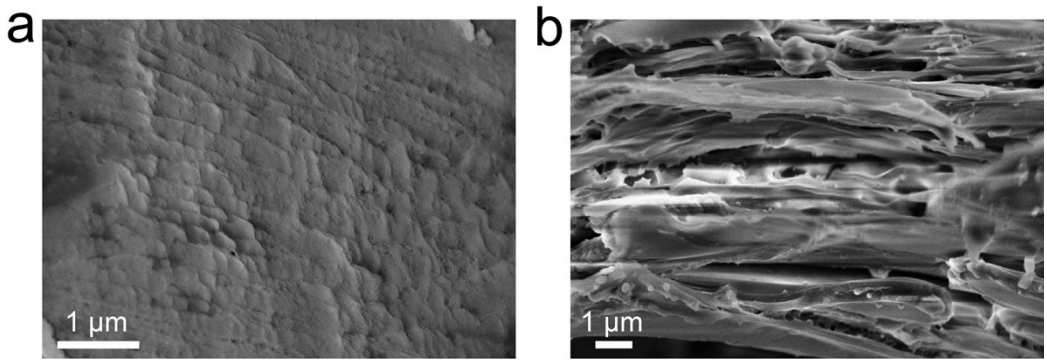

Figure S27. SEM images of $Ti_3C_2S_x$ elextrode at the (a) fully discharged and (b) charged states.

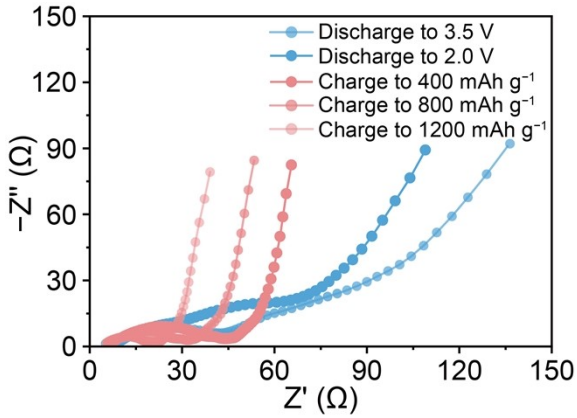

Figure S28. Nyquist plots of the Li–Cl_2@$Ti_3C_2S_x$ battery at different discharging/charging states.

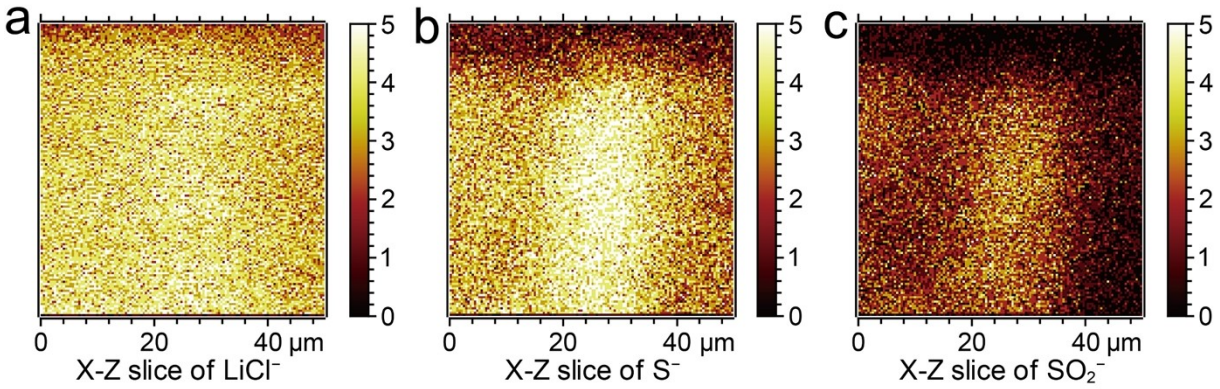

Figure S29. High-resolution chemical maps of the (a) $LiCl^{-}$, (b) S^{-}, and (c) SO_2^{-} secondary ion signals of discharged $Ti_3C_2S_x$ electrode.

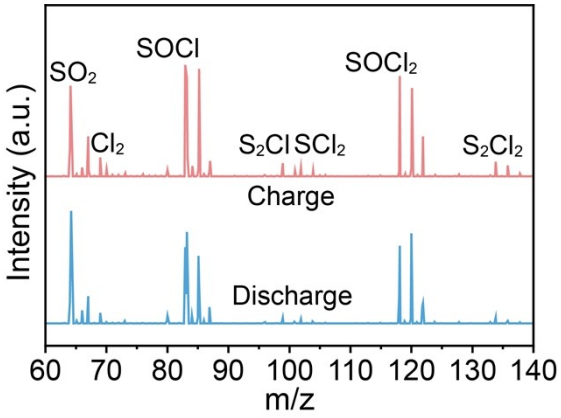

Figure S30. Mass spectrometry of the charged and discharged electrodes.

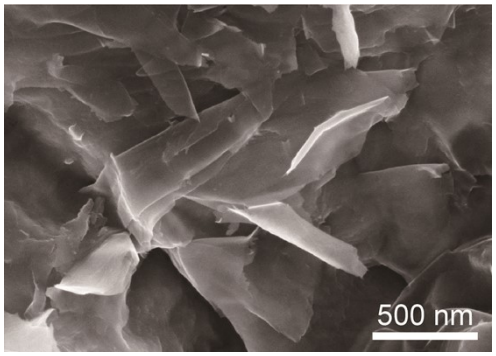

Figure S31. SEM image of exfolited $Ti_3C_2S_x$ nanosheets.

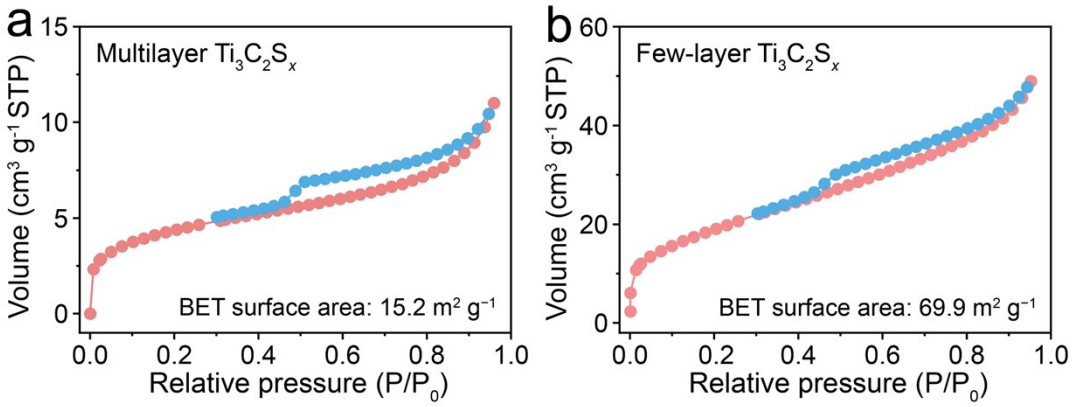

Figure S32. N_2 adsorption/desorption curves of (a) multilayer $Ti_3C_2S_x$ and (b) few-layer $Ti_3C_2S_x$.

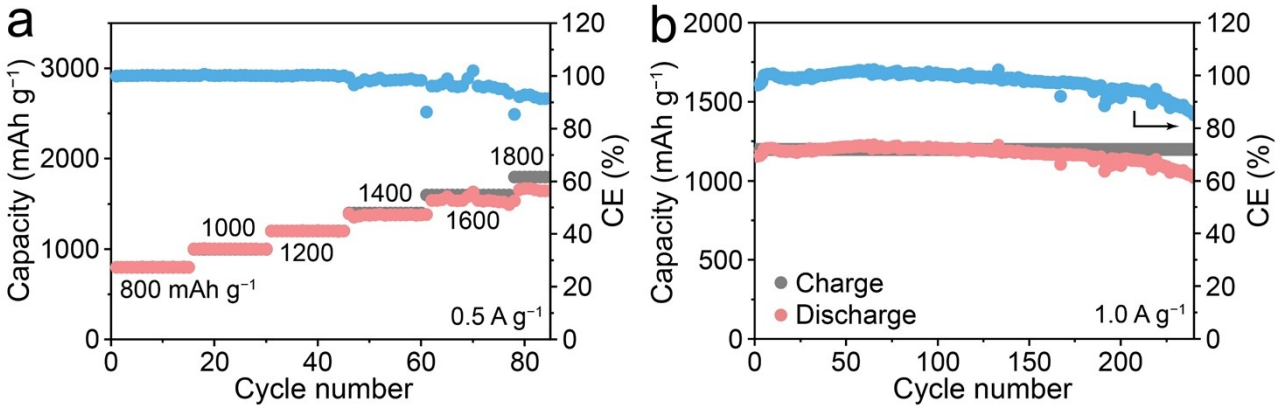

Figure S33. Electrochemical performance of exfolited $Ti_3C_2Se_x$ nanosheets.

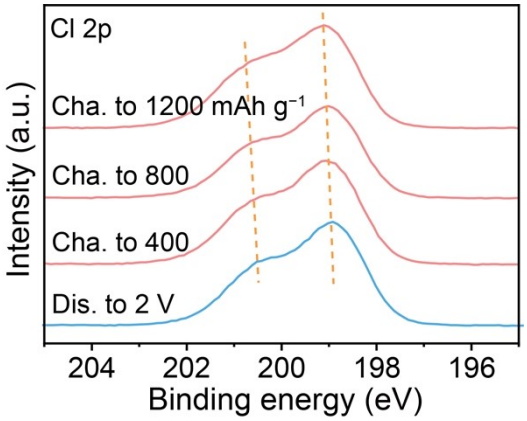

Figure S34. High-resolution Cl 2p XPS spectra recorded for the $Ti_3C_2S_x$ electrode at different states.

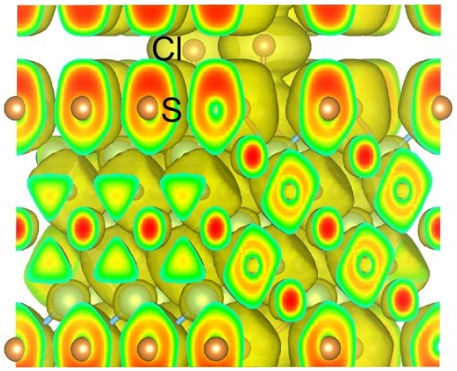

Figure S35. 3D ELF analysis of $Ti_3C_2S_x$.

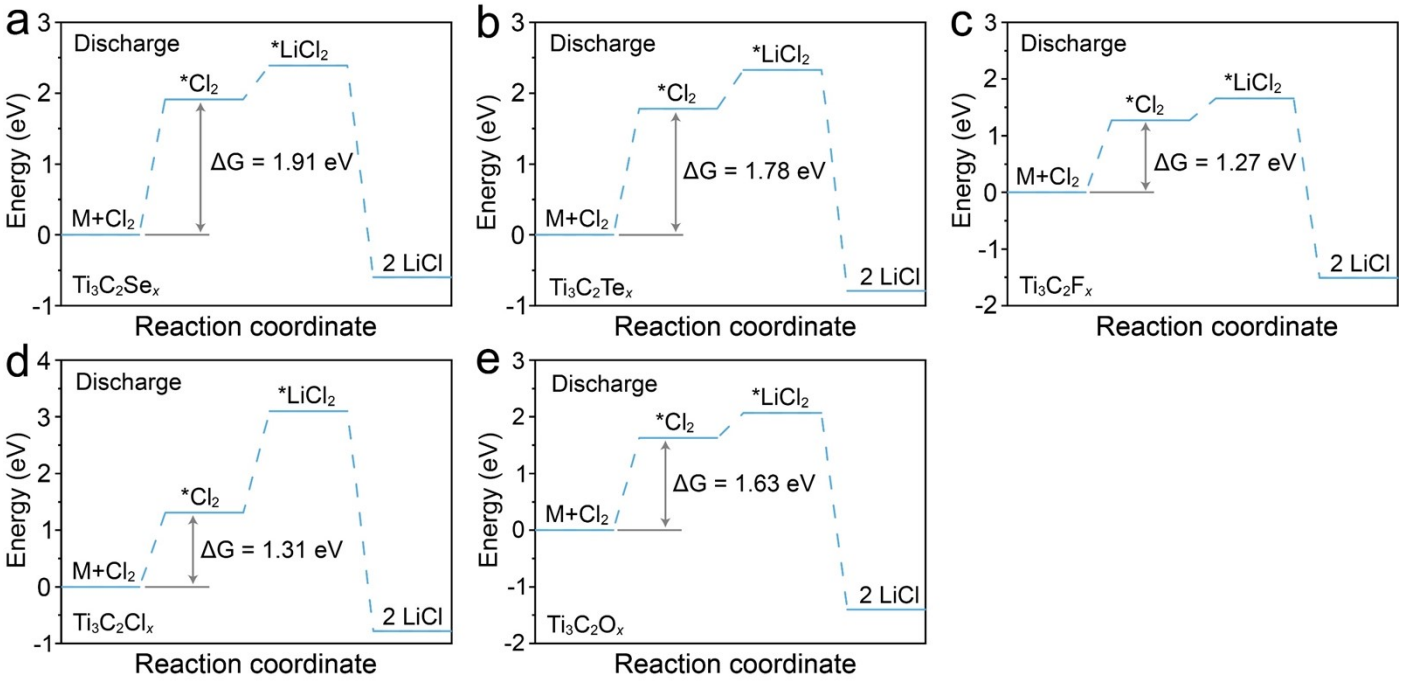

Figure S36. Gibbs free energy for the conversion of Cl_2 to LiCl during discharge.

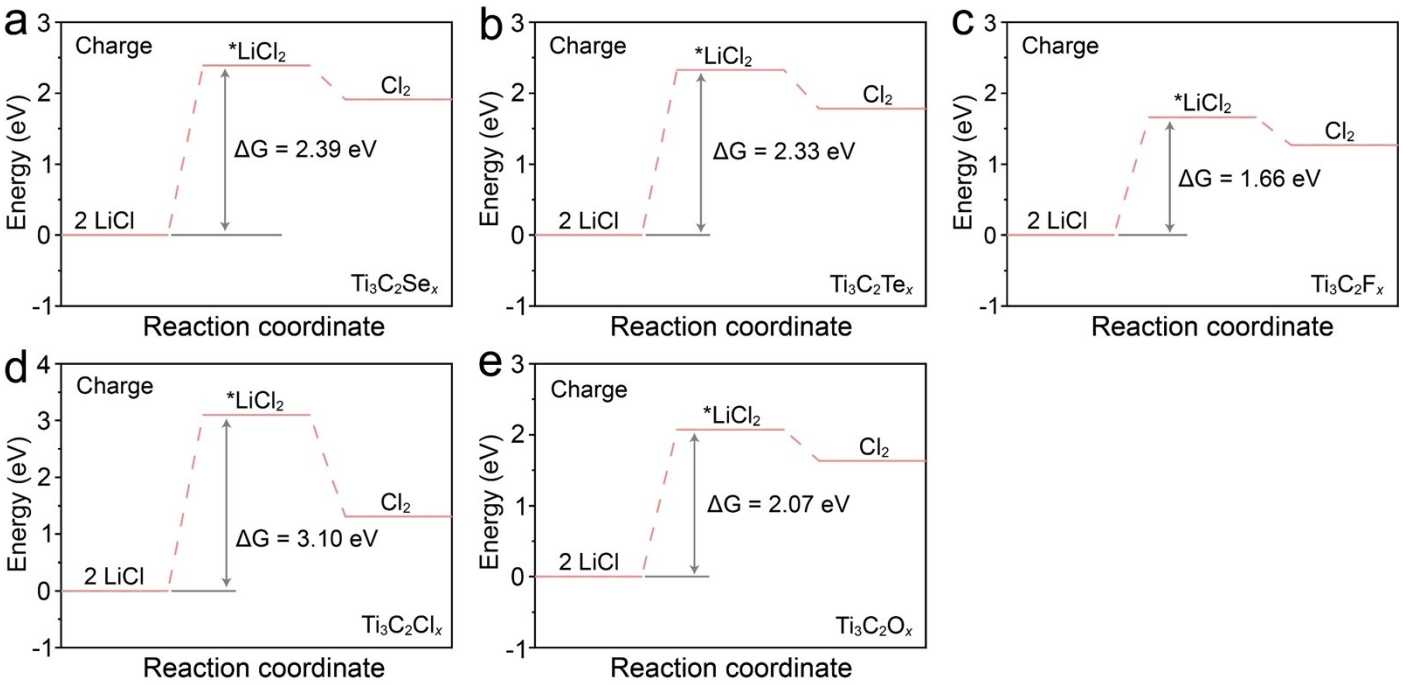

Figure S37. Gibbs free energy for the conversion of LiCl to Cl_2 during charge.

Table S1. Electrochemical performance comparison of Li–Cl_2 batteries at room temperature.

Cathode materias	Anodes	Cycling performance	Accumulated capacity	References
$Ti_3C_2S_x$ MXene	**Li**	**1300 cycles (1200 mAh g^{-1}, 3.0 A g^{-1})**	**1.5 × 10^6 mAh g^{-1}**	**This work**
Graphene	Li	750 cycles (500 mAh g^{-1}, 1.5 A g^{-1})	3.75 × 10^5 mAh g^{-1}	1
Co-nitrogen-dope carbon	Li	600 cycles (500 mAh g^{-1}, 1.5 A g^{-1})	3.0 × 10^5 mAh g^{-1}	2
COF-NH_2	Li	100 cycles (2500 mAh g^{-1}, 0.8 A g^{-1})	2.5 × 10^5 mAh g^{-1}	3
Defective graphite	Li	140 cycles (600 mAh g^{-1}, 0.1 A g^{-1})	8.4 × 10^4 mAh g^{-1}	4
CC_3-POC	Li	160 cycles (2000 mAh g^{-1}, 1.0 A g^{-1})	3.2 × 10^5 mAh g^{-1}	5
UiO-66-NH_2	Li	500 cycles (1000 mAh g^{-1}, 1.0 A g^{-1})	5.0 × 10^5 mAh g^{-1}	6
Nitrogen-doped carbon	Li	460 cycles (500 mAh g^{-1}, 1.5 A g^{-1})	2.3 × 10^5 mAh g^{-1}	7
Amorphous carbon nanospheres	Li	120 cycles (500 mAh g^{-1}, 0.1 A g^{-1})	6.0 × 10^4 mAh g^{-1}	8

Table S2. Electrochemical performance comparison of Li metal batteries at subzero temperature.

Cathode materias	Anodes	Electrolytes	Temperature	Cycling performance	References
$Ti_3C_2S_x$ MXene	**Li**	**2 M $AlCl_3$, 2 M LiCl, 2 wt% LiTFSI, and 2 wt% LiFSI in $SOCl_2$**	**−60 °C**	**1200 cycles (1200 mAh g^{-1}, 0.8 A g^{-1})**	**This work**
Graphene	Li	4 M $AlCl_3$, 2 wt% LiTFSI, and 2 wt% LiFSI in $SOCl_2$	−40 °C	100 cycles (500 mAh g^{-1}, 0.1 A g^{-1})	1
Co-nitrogen-dope carbon	Li	4 M $AlCl_3$, 2 wt% LiTFSI, and 2 wt% LiFSI in $SOCl_2$	−40 °C	650 cycles (500 mAh g^{-1}, 0.5 A g^{-1})	2
$COF\text{-}NH_2$	Li	2 M $AlCl_3$, 2 M LiCl, 2 wt% LiTFSI, and 2 wt% LiFSI in $SOCl_2$	−20 °C	200 cycles (2000 mAh g^{-1}, 0.3 A g^{-1})	3
CC_3-POC	Li	2 M $AlCl_3$, 2 M LiCl, 2 wt% LiTFSI, and 2 wt% LiFSI in $SOCl_2$	−20 °C	200 cycles (2000 mAh g^{-1}, 0.3 A g^{-1})	5
$UiO\text{-}66\text{-}NH_2$	Li	4 M $AlCl_3$, 4 wt% LiTFSI, and 4 wt% LiFSI in $SOCl_2$	−25 °C	300 cycles (1000 mAh g^{-1}, 0.45 A g^{-1})	6
Nitrogen-doped carbon	Li	4 M $AlCl_3$, 2 wt% LiTFSI, and 2 wt% LiFSI in $SOCl_2$	−20 °C	1500 cycles (500 mAh g^{-1}, 1.5 A g^{-1})	7
CO_2 activated porous carbon	Li	1 M $AlCl_3$, 0.95 M LiCl, and 0.05 M LiFSI in $SOCl_2$	−40 °C	130 cycles (1200 mAh g^{-1}, 0.1 A g^{-1})	9
$LiFePO_4$	Li	1.0 M LiFSI, 0.1 M each of LiTFSI, $LiPF_6$, LiDFOB, and $LiNO_3$ in DOL	−20 °C	500 cycles (0.1 C)	10
$LiNi_{0.83}Co_{0.11}Mn_{0.06}O_2$	Li	1.0 M LiFSI and 0.02 M $LiNO_3$ in DME and TTE (3:7)	−20 °C	500 cycles (0.2 C)	11
$LiNi_{0.6}Co_{0.2}Mn_{0.2}O_2$	Li	1.0 M $LiPF_6$, 0.5 wt% AIBN, and 1.5 wt% PETEA in TFEA, EA-2F, and FEC	−20 °C	700 cycles (0.25 C)	12
$LiNi_{0.83}Mn_{0.05}Co_{0.12}O_2$	Li	1.0 M LiFSI in DME, DMC, and TTE (1.2:1.8:3)	−40 °C	100 cycles (0.1 C)	13
$LiNi_{0.90}Co_{0.05}Mn_{0.05}O_2$	Li	1.0 M $LiPF_6$ in EC, DEC, and DMC(1:1:1)	−30 °C	1000 cycles (0.1 C)	14

References

1. J. Han, X. Wei, G. Ma, H. Wang, Y. Sun, Z. Liu, L. Zhao, C. Ma, Q. Liu, W. Feng, D. Kong, W. Lv, Q. Yang, L. Zhi, *Energy Environ. Sci.* **2025**, *18*, 8052–8065.
2. P. Li, C. Ma, Y. Wang, S. Zhai, G. Ma, D. Kong, Z. Li, *Adv. Mater.* **2025**, *37*, 2418990.
3. Y. Xu, M. Wang, M. Sajid, Y. Meng, Z. Xie, L. Sun, J. Jin, W. Chen, S. Zhang, *Angew Chem., Int. Ed*. **2024**, *63*, e202315931.
4. G. Zhu, P. Liang, C. Huang, C. Huang, Y. Li, S. Wu, J. Li, F. Wang, X. Tian, W. Huang, S. Jiang, W. Huang, H. Chen, M. Lin, B. Hwang, H. Dai, *J. Am. Chem. Soc.* **2022**, *144*, 22505–22513.
5. Y. Xu, S. Zhang, M. Wang, Y. Meng, Z. Xie, L. Sun, C. Huang, W. Chen, *J. Am. Chem. Soc.* **2023**, *145*, 27877–27885.
6. Y. Xu, L. Jiao, J. Ma, P. Zhang, Y. Tang, L. Liu, Y. Liu, H. Ding, J. Sun, M. Wang, Z. Li, H. Jiang, W. Chen, *Joule* **2023**, *7*, 515–528.
7. X. Wei, D. Kong, W. Feng, F. Cao, C. Ma, J. Yang, J. Han, L. Wang, G. Ma, H. Wang, Y. Sun, Z. Liu, L. Wei, L. Zhi, *Adv. Energy Mater.* **2025**, *15*, 2501333.
8. G. Zhu, X. Tian, H. Tai, Y. Li, J. Li, H. Sun, P. Liang, M. Angell, C. Huang, C. Ku, W. Hung, S. Jiang, Y. Meng, H. Chen, M. Lin, B. Hwang, H. Dai, *Nature* **2021**, *596*, 525–530.
9. P. Liang, G. Zhu, C. Huang, Y. Li, H. Sun, B. Yuan, S. Wu, J. Li, F. Wang, B. Hwang, H. Dai, *Adv. Mater.* **2024**, *36*, 2307192.
10. J. Guo, W. Zou, Y. Song, X. Zhu, H. Zhou, W. Zhang, F. Zhou, T. Li, *Angew Chem., Int. Ed*. **2025**, *64*, e202511612.
11. Z. Xiao, X. Liu, F. Hai, Y. Li, D. Han, X. Gao, Z. Huang, Y. Liu, Z. Li, W. Tang, Y. Wu, S. Passerini, *Angew Chem., Int. Ed.* **2025**, *64*, e202503693.
12. Y. Wei, H. Wang, X. Lin, T. Wang, Y. Cui, Y. Huang, J. Yang, T. Liu, Y. Ren, X. Fan, H. Xu, Y. Huang, *Energy Environ. Sci*. **2025**, *18*, 786–798.
13. X. Meng, X. Zhang, L. Shi, Z. Chen, J. Meng, F. Ding, X. Liu, B. Zhang, Q. Wang, L. Mai, C. Niu, *Energy Environ. Sci.* **2025**, *18*, 9907–9916.
14. S. Dong, L. Shi, Y. Zhang, S. Geng, Z. Qiang, B. Deng, F. Sun, H. Huo, G. Yin, S. Lou, *Angew Chem., Int. Ed*. **2025**, *64*, e202506750.
15. J. P. Perdew, K. Burke, M. Ernzerhof, *Phys. Rev. Lett.* **1996**, *77*, 3865–3868.
16. P. E. Blöchl, *Phys. Rev. B* **1994**, *50*, 17953–17979.
17. G. Kresse, D. Joubert, *Phys. Rev. B*. **1999**, *59*, 1758–1775.
18. G. Kresse, J. Furthmüller, *Phys. Rev. B* **1996**, *54*, 11169–11186.
19. G. Kresse, J. Furthmüller, *Comput. Mater. Sci.* **1996**, *6*, 15–50.
20. S. Grimme, S. Ehrlich, L. Goerigk, *J. Comput. Chem.* **2011**, *32*, 1456–1465.
21. V. Wang, N. Xu, J. Liu, G. Tang, W. Geng, *Comput. Phys. Commun.* **2021**, *267*, 108033.

22. K. Momma, F. Izumi, *J. Appl. Crystallogr.* **2011**, *44*, 1272–1276.